Supplementary Information
Hydrodynamic pursuit by cognitive self-steering microswimmers

Segun Goh,[1,*] Roland G. Winkler,[1,†] and Gerhard Gompper[1,‡]

[1] *Theoretical Physics of Living Matter, Institute of Biological Information Processing and Institute for Advanced Simulation, Forschungszentrum Jülich, 52425 Jülich, Germany*

(Dated: June 6, 2023)

S-I. MULTI-PARTICLE COLLISION DYNAMICS (MPC)

A. Fluid dynamics

A MPC fluid consists of N point particles of mass m, whose dynamics proceeds in alternating streaming and collision steps. In the streaming step, the particles move ballistically according to

$$\boldsymbol{r}_i(t+h) = \boldsymbol{r}_i(t) + h\boldsymbol{v}_i, \tag{S1}$$

where $\boldsymbol{r}_i$ and $\boldsymbol{v}_i$ $(i = 1, \dots, N)$ denote the positions and the velocities of the MPC particles, and the collision time h is the time interval between collisions. Coarse-grained interactions between MPC particles are modeled by a momentum conserving, stochastic process in the collision step, for which the whole system is divided into cubic collision cells of side length of a, containing $\langle N_c \rangle$ MPC particles on average. These cells are randomly shifted to ensure Galilean invariance [1]. In the stochastic rotation dynamics variant of MPC [2, 3] with angular momentum conservation [4, 5] (MPC-SRD+a), the velocities after a collision are given by

$$\boldsymbol{v}_i(t+h) = \boldsymbol{v}_{\rm cm}(t) + \mathbf{D}(\alpha_c)\,\boldsymbol{v}_{i,c} + \boldsymbol{\omega}_c(t) \times \boldsymbol{r}_{i,c}(t). \tag{S2}$$

Here, $\boldsymbol{r}_{i,c} = \boldsymbol{r}_i - \boldsymbol{r}_{\rm cm}$ and $\boldsymbol{v}_{i,c} = \boldsymbol{v}_i - \boldsymbol{v}_{\rm cm}$ are the positions and velocities with respect to the center-of-mass position $\boldsymbol{r}_{\rm cm} = \sum_{i=1}^{N_c} \boldsymbol{r}_i/N_c$ and the center-of-mass velocity $\boldsymbol{v}_{\rm cm} = \sum_{i=1}^{N_c} \boldsymbol{v}_i/N_c$. The angular velocity is given by

$$\boldsymbol{\omega}_c = m\mathbf{I}_c^{-1} \sum_{i=1}^{N_c} \big(\boldsymbol{r}_{i,c} \times (\boldsymbol{v}_{i,c} - \mathbf{D}(\alpha_c)\,\boldsymbol{v}_{i,c})\big), \tag{S3}$$

where $\mathbf{D}(\alpha_c)$ denotes the rotation matrix for a rotation by an angle α_c around a randomly orientated axis of the collision cell, and $\mathbf{I}_c$ is the moment-of-inertia tensors of the MPC particles in the collision cell. A constant local temperature is maintained by a cell-level canonical thermostat (Maxwell-Boltzmann scaling (MBS) thermostat) [6, 7].

* s.goh@fz-juelich.de
† r.winkler@fz-juelich.de
‡ g.gompper@fz-juelich.de

S-II. SQUIRMER DYNAMICS

A. Rigid body dynamics

A squirmer is consider as a spherical rigid body with translational and rotational degrees of freedom. Newton's equations of motion for the *translational* motion are solved by the velocity-Verlet algorithm, which yields

$$\boldsymbol{r}(t+\Delta t) = \boldsymbol{r}(t) + \boldsymbol{u}(t)\Delta t + \frac{\Delta t^2}{2M}\boldsymbol{F}(t), \tag{S4}$$

$$\boldsymbol{u}(t+\Delta t) = \boldsymbol{u}(t) + \frac{\Delta t}{2M}\left[\boldsymbol{F}(t) + \boldsymbol{F}(t+\Delta t)\right], \tag{S5}$$

for the squirmers' position $\boldsymbol{r}$ and velocity $\boldsymbol{v}$, with the force $\boldsymbol{F}$ between squirmers, e.g., by the Lennard-Jones potential Eq. (22), and the time step $\Delta t = 0.1h$, where $h = 0.02\,a\sqrt{m/(k_BT)}$ is the collision time of the MPC fluid [8].

The equations of motion of the *rotational* dynamics are solved via quaternions $\boldsymbol{q} = (q_0, q_1, q_2, q_3)^T$ [8–10] . In the body fixed reference frame, the equations of motion are

$$\dot{\boldsymbol{q}} = \frac{1}{2}\mathbf{Q}(\boldsymbol{q}) \begin{pmatrix} 0 \\ \boldsymbol{\Omega}^b \end{pmatrix}, \tag{S6}$$

$$\ddot{\boldsymbol{q}} = \frac{1}{2}\mathbf{Q}(\dot{\boldsymbol{q}}) \begin{pmatrix} 0 \\ \boldsymbol{\Omega}^b \end{pmatrix} + \frac{1}{2}\mathbf{Q}(\dot{\boldsymbol{q}}) \begin{pmatrix} 0 \\ \dot{\boldsymbol{\Omega}}^b \end{pmatrix}, \tag{S7}$$

with the matrix

$$\mathbf{Q}(\boldsymbol{q}) = \begin{pmatrix} q_0 & -q_1 & -q_2 & -q_3 \\ q_1 & q_0 & -q_3 & q_2 \\ q_2 & q_3 & q_0 & -q_1 \\ q_3 & -q_2 & q_1 & q_0 \end{pmatrix}, \tag{S8}$$

the angular velocity $\boldsymbol{\Omega}^b$ in the body fixed frame, and its equations of motion in Cartesian coordinates $\alpha \in \{x, y, z\}$

$$\frac{d\Omega^b_\alpha}{dt} = I_\alpha^{-1}\left[T^b_\alpha + (I_\beta - I_\gamma)\Omega^b_\beta\Omega^b_\gamma\right]. \tag{S9}$$

Here, $\boldsymbol{T}$ is the torque on the sphere and $\mathbf{I}$ its moment of inertia tensor. Equations (S9) are Euler's equations of the rigid body dynamics and hold for $(\alpha, \beta, \gamma) = (x, y, z), (y, z, x)$, and (z, x, y). The steric interactions between the squirmers of the main text do not exert any torque. Hence, $d\boldsymbol{\Omega}^b(t)/dt = 0$ for the homogeneous sphere, where its inertia tensor is diagonal and

$I_x = I_y = I_x = 2MR_{\rm sq}/5$. The equations (S6) and (S7) are solved by the Taylor expansion

$$\boldsymbol{q}(t+\Delta t) = (1-\tilde{\lambda})\boldsymbol{q}(t) + \dot{\boldsymbol{q}}(t)\Delta t + \frac{\Delta t^2}{2}\ddot{\boldsymbol{q}}(t), \tag{S10}$$

where the Lagrange multiplier $\tilde{\lambda}$ ensures the constraint $\boldsymbol{q}^2 = 1$ and is given by

$$\tilde{\lambda} = 1 - \dot{\boldsymbol{q}}^2\Delta t^2/2 - \sqrt{1 - \dot{\boldsymbol{q}}^2\Delta t^2 - \dot{\boldsymbol{q}}\cdot\ddot{\boldsymbol{q}}\Delta t^3 - (\ddot{\boldsymbol{q}}^2 - \dot{\boldsymbol{q}}^4)\Delta t^4/4}. \tag{S11}$$

The translational, $\boldsymbol{v}^s$, and angular velocity, $\boldsymbol{\Omega}^s$, in the laboratory frame follow from the relations

$$\boldsymbol{v}^s = \mathbf{D}^T\boldsymbol{v}^b, \tag{S12}$$

$$\boldsymbol{\Omega}^s = \mathbf{D}^T\left(\mathbf{I}^b\right)^{-1}\mathbf{D}\boldsymbol{L}^s, \tag{S13}$$

with

$$\mathbf{D} = \tag{S14}$$

$$\begin{pmatrix} q_0^2+q_1^2-q_2^2-q_3^2 & 2(q_1q_2+q_0q_3) & 2(q_1q_3-q_0q_2) \\ 2(q_1q_2-q_0q_3) & q_0^2-q_1^2+q_2^2-q_3^2 & 2(q_2q_3+q_0q_1) \\ 2(q_1q_3+q_0q_2) & 2(q_2q_3-q_0q_1) & q_0^2-q_1^2-q_2^2+q_3^2 \end{pmatrix} \tag{S15}$$

and the angular momentum of the sphere $\boldsymbol{L}^s$.

B. Squirmer-MPC fluid coupling

Coupling between the sphere and the MPC fluid occurs during the streaming and collision step, with a linear and angular momentum transfer. During the streaming step, a sphere collides with various MPC particles. Since the total change in (angular) momentum of a sphere during one streaming step is small, its collisions with MPC particles are perform in a coarse-grained manner [8, 11]. For the streaming step at time t, the sphere's position, velocity, orientation, and angular velocity at the time $t+h$ are determined under the assumption that there is no interaction with MPC particles, but potentially with other squirmers. Subsequently, all MPC particles are streamed, i.e., their positions are updated according to Eq. (S1), where a certain fraction of MPC particles penetrates the sphere. These particles are identified, translated onto the sphere's surface, and the momentum transfer

$$\boldsymbol{J}_i^{\rm str} = 2m\left\{\boldsymbol{v}_i - \boldsymbol{u} - \boldsymbol{\Omega}\times(\boldsymbol{r}_i-\boldsymbol{r}) - \mathbf{D}^T\boldsymbol{u}^b_{\rm sq}[\mathbf{D}(\boldsymbol{r}_i-\boldsymbol{r})]\right\} \tag{S16}$$

is determined applying the bounce-back rule and taking into account the squirmer surface fluid velocity $\boldsymbol{u}^b_{sq}$. There velocities are correspondingly updated according to

$$\boldsymbol{v}_i' = \boldsymbol{v}_i - \boldsymbol{J}_i^{\rm str}/m. \tag{S17}$$

As a consequence of the elastic collisions, the center-of-mass velocity and rotation frequency of a colloid are finally given by

$$\boldsymbol{u}(t+h)' = \boldsymbol{u}(t+h) + \boldsymbol{J}/M, \tag{S18}$$

$$\boldsymbol{\Omega}(t+h)' = \boldsymbol{\Omega}(t+h) + \mathbf{D}^T\left(\mathbf{I}^b\right)^{-1}\mathbf{D}\boldsymbol{L}, \tag{S19}$$

where $\boldsymbol{J} = \sum_i \boldsymbol{J}_i$ is total momentum transfer by the MPC fluid and $\boldsymbol{L} = \sum_i(\boldsymbol{r}_i(t+h) - \boldsymbol{r}(t+h))\times\boldsymbol{J}_i$ is the respective angular momentum transfer.

In the collision step, phantom particles are distributed inside a sphere, with the same mass and density as the fluid particles [1, 11]. The phantom particle positions $\boldsymbol{r}_i^p$ are uniformly distributed inside the sphere with the velocities

$$\boldsymbol{v}_i^p = \boldsymbol{u} + \boldsymbol{\Omega}\times(\boldsymbol{r}_i - \boldsymbol{r}) + \boldsymbol{u}_{\rm sq}(\boldsymbol{r}_i) + \boldsymbol{v}_{R,i}. \tag{S20}$$

The Cartesian components of $\boldsymbol{v}_{R,i}$ are Gaussian-distributed random numbers with zero mean and variance $\sqrt{k_BT/m}$. The squirming velocity $\boldsymbol{u}_{\rm sq}(\boldsymbol{r}_i)$ is determined by Eqs. (5), (6) of the main text, with the phantom particle position $\boldsymbol{r}_i$ projecting onto the sphere's surface. As a result of MPC collisions, a sphere's linear and angular momentum change by $\boldsymbol{J}_i^p = m(\boldsymbol{v}'^p_i - \boldsymbol{v}^p_i)$ and $\boldsymbol{L}_i^p = (\boldsymbol{r}_i^p - \boldsymbol{r})\times\boldsymbol{J}_i^p$, where $\boldsymbol{v}'^p_i$ and $\boldsymbol{v}^p_i$ are the phantom particles' velocities after and before the MPC collision. Hence, the colloid translational and angular velocity become

$$\boldsymbol{u}' = \boldsymbol{u} + \boldsymbol{J}^p/M, \tag{S21}$$

$$\boldsymbol{\Omega}' = \boldsymbol{\Omega} + \mathbf{D}^T\left(\mathbf{I}^b\right)^{-1}\mathbf{D}\boldsymbol{L}^b. \tag{S22}$$

S-III. STRAIGHT TRAJECTORY

A. Target-pursuer configurations

1. *Orientation vectors*

Figure S1**a** and Fig. 2**d** in the main text depict orientational alignment parameters of the unit vectors $\boldsymbol{e}_p$, $\boldsymbol{e}_t$, and $\boldsymbol{e}_c$ as a function of Ω. In successful cases, the average $\langle\boldsymbol{e}_p\cdot\boldsymbol{e}_c\rangle$, directly affected by self-steering, is always larger than 0.7 (Fig. S1**a**-I). In contrast, $\boldsymbol{e}_t$ and $\boldsymbol{e}_c$ are not necessarily parallel, especially for pullers, see Fig. S1**a**-II. A similar behavior is obtained for $\langle\boldsymbol{e}_t\cdot\boldsymbol{e}_p\rangle$ in Fig. 2**d** of the main text. In any case, the alignment parameters approach unity for large maneuverability $\Omega \gtrsim 4\mathrm{Pe}$. Notably, as shown in Fig. S1**a**-III, the average distance remains unchanged in spite of the misalignment in the propulsion directions for small Ω.

The average values of the orientational alignment parameters for a fixed ratio of $\Omega = 4\mathrm{Pe}$ are displayed in Fig. S1**b** as a function of the target propulsion speed ratio $\alpha = v_t/v_p$. For this large maneuverability, $\langle\boldsymbol{e}_p\cdot\boldsymbol{e}_c\rangle \approx 1$ (Fig. S1**b**-I). On the other hand, a strong decoupling of

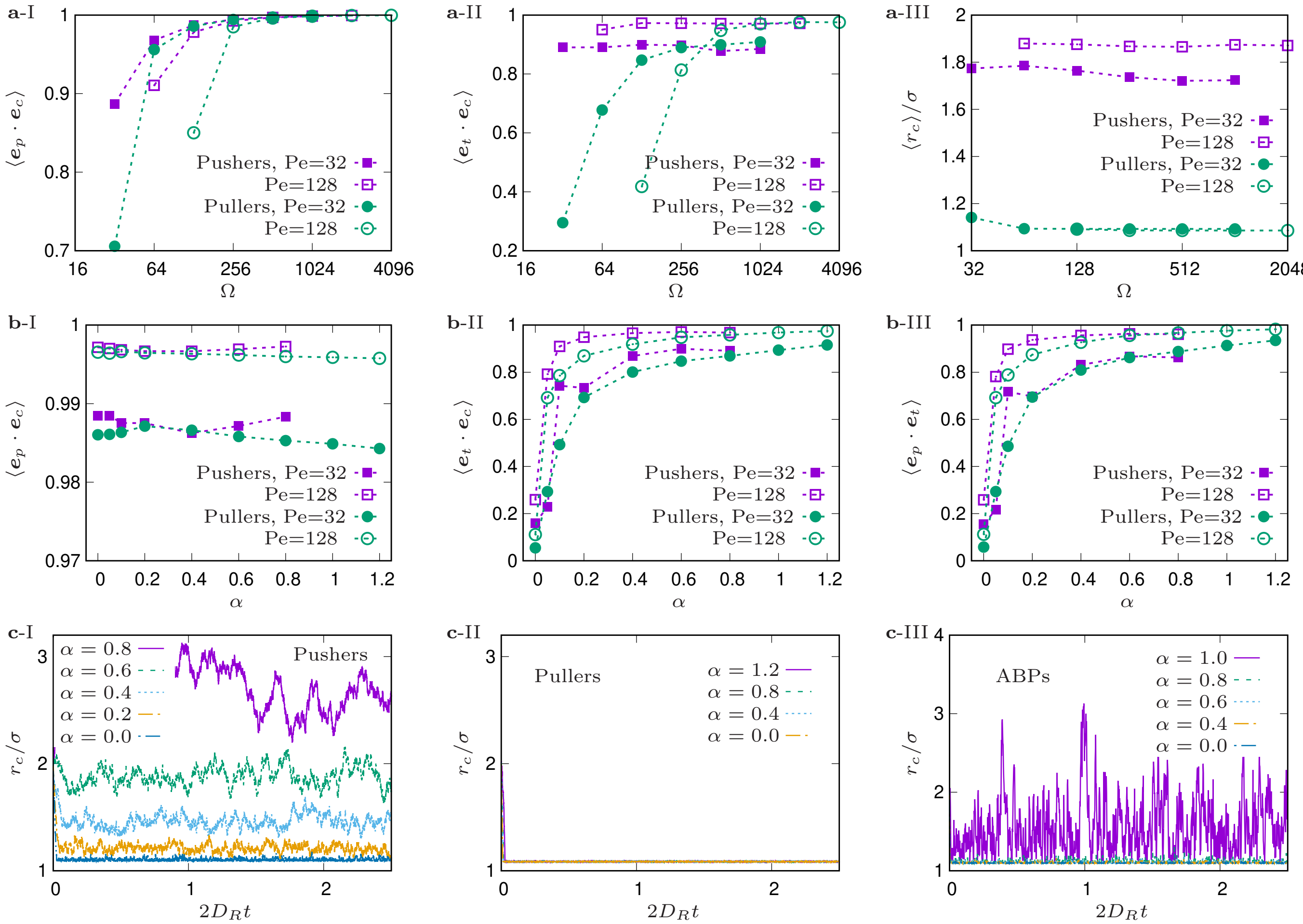

FIG. S1. **a** Orientational alignment parameters (I) $\langle \boldsymbol{e}_p \cdot \boldsymbol{e}_c \rangle$ and (II) $\langle \boldsymbol{e}_t \cdot \boldsymbol{e}_c \rangle$ between the pursuer and target propulsion directions, and (III) average distance between the squirmers as a function of the maneuverability Ω for $\alpha = 0.6$. The pursuit dynamics in simulations with a maneuverability four times smaller than the minimum values shown in the figure failed, which indicates that $\Omega \approx \mathrm{Pe}/2$ corresponds to a minimal maneuverability for a successful pursuit. **b** Orientational alignment parameters $\langle \boldsymbol{e}_p \cdot \boldsymbol{e}_c \rangle$, $\langle \boldsymbol{e}_p \cdot \boldsymbol{e}_c \rangle$, and $\langle \boldsymbol{e}_p \cdot \boldsymbol{e}_c \rangle$ as a function of α, where $\Omega = 4\,\mathrm{Pe}$. **c** Examples of the time evolution of r_c for (I) pushers, (II) pullers (II), and (III) ABPs and the indicated α values.

$\boldsymbol{e}_t$ with $\boldsymbol{e}_c$ as well as with $\boldsymbol{e}_p$ is observed in Figs. S1**b**-II and **b**-III for small α, where the target is pushed by the faster pursuer rather than self-propelled due to the low propulsion velocity v_t. Therefore, the rotational motion of the target does not contribute to the direction of coherent movement of the target-pursuer pair.

2. *Distance*

The time evolution of the distance between a target and a pursuer is displayed in Fig. S1**c** for pushers, pullers, and ABPs. In the case of pullers, a target and a pursuer always touch each other if the pursuit is successful, while a pusher pursuer can never reach the target for $\alpha \geq 0.4$. This reflects that dynamics of the squirmers is qualitatively different from that of ABPs, where, in the latter case, intermittent touching and detachment are observed due to thermal noises.

3. *Far-field approximation*

The far-field approximation of the hydrodynamic interaction predicts the asymptotic behavior [12, 13]

$$\frac{\boldsymbol{U}_{t,F}}{v_t} = \boldsymbol{e}_t - \frac{3}{16\alpha}\frac{\sigma^2}{r_c^2}\beta\{3(\boldsymbol{e}_p \cdot \boldsymbol{e}_c)^2 - 1\}\,\boldsymbol{e}_c, \tag{S23}$$

$$\frac{\boldsymbol{U}_{p,F}}{v_p} = \boldsymbol{e}_p + \frac{3\alpha}{16}\frac{\sigma^2}{r_c^2}\beta\{3(\boldsymbol{e}_t \cdot \boldsymbol{e}_c)^2 - 1\}\,\boldsymbol{e}_c. \tag{S24}$$

For stable cooperative motion at a given distance, the pursuer has to move faster than the target, i.e., $|\boldsymbol{U}_{p,F}| > |\boldsymbol{U}_{t,F}|$ so that the distance between them decreases over time. With the assumption $\boldsymbol{e}_p = \boldsymbol{e}_t = \boldsymbol{e}_c$ for head-to-tail configurations corresponding to $\boldsymbol{U}_{p,F} \parallel \boldsymbol{U}_{t,F}$, together

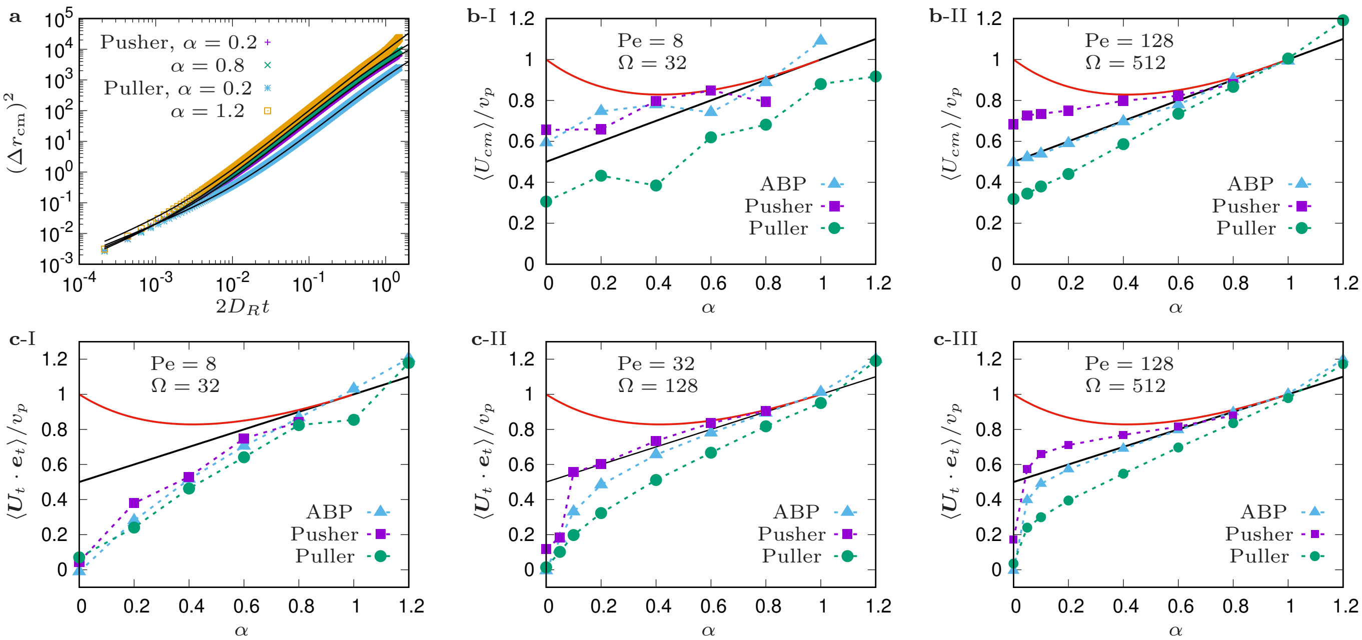

FIG. S2. **a** Center-of-mass mean-square displacement of squirmers as a function of time for Pe = 32 and various velocity ratios α. The black solid lines are fits of Eq. (S31). **b** Average values of the center-of-mass speed $U_{\rm cm}$ for (I) Pe = 8 and (II) Pe = 128. **c** Effective swim speed $\langle \boldsymbol{U}_t \cdot \boldsymbol{e}_t\rangle$ of the target for (I) Pe = 8, (II) Pe = 32, and (III) Pe = 128. The red lines represent the noise-free far-field approximation of Eq. (S29) and black lines the target-pursuer average speed $(v_p + v_t)/2 = v_p(1+\alpha)/2$.

with the far-field approximation of Eqs. (S23) and (S24), we obtain

$$1 + \frac{3\alpha}{8}\frac{\sigma^2}{r_c^2}\beta > \alpha - \frac{3}{8}\frac{\sigma^2}{r_c^2}\beta, \tag{S25}$$

which implies

$$\alpha < \frac{8r_c^2/(3\sigma^2) + \beta}{8r_c^2/(3\sigma^2) - \beta}. \tag{S26}$$

A stable configuration is achieved at the distance $r_c = r_0$, where $\boldsymbol{U}_{t,F} = \boldsymbol{U}_{p,F}$, again with the assumption $\boldsymbol{e}_p = \boldsymbol{e}_t = \boldsymbol{e}_c$. Replacing the inequality with an equal sign in Eq. (S25), we obtain the estimate of stationary-state pursuer-target distance

$$r_c < r_0 = \sigma\sqrt{\frac{3\beta(\alpha+1)}{8(\alpha-1)}}. \tag{S27}$$

Then, replacement of $r_c = r_0$ in Eq. (S23) or Eq. (S24) yields

$$\boldsymbol{U}_{t,F} = \boldsymbol{U}_{p,F} = \frac{1+\alpha^2}{1+\alpha} v_p\, \boldsymbol{e}_p, \tag{S28}$$

or

$$\bar{v} = |\boldsymbol{U}_{t,F}| = |\boldsymbol{U}_{p,F}| = \frac{1+\alpha^2}{1+\alpha} v_p. \tag{S29}$$

B. Propulsion speed

1. *Center-of-mass speed*

The center-of-mass speed of a squirmer pair is determined via their center-of-mass mean-square displacement (MSD) [14]

$$\Delta \boldsymbol{r}_{\rm cm}^2 = \langle (\boldsymbol{r}_{\rm cm}(t) - \boldsymbol{r}_{\rm cm}(0))^2 \rangle, \tag{S30}$$

where $\boldsymbol{r}_{\rm cm} = (\boldsymbol{r}_t + \boldsymbol{r}_p)/2$. The center-of-mass velocity $U_{\rm cm}$ follows from the fit of the MSD by the analytical expression for an ABP [14]

$$\left\langle (\boldsymbol{r}_{\rm cm}(t) - \boldsymbol{r}_{\rm cm}(0))^2 \right\rangle = \frac{3k_BT}{\gamma_T} t + \frac{2U_{\rm cm}^2}{\gamma_R^2}(\gamma_R t + e^{-\gamma_R t} - 1), \tag{S31}$$

where γ_T is the translational friction coefficient and $\gamma_R = 2D_R'$ is related with an effective rotational coefficient coefficient D_R'. Figure. S2**a** shows various examples of fitted data, and Fig. S2**b** presents center-of-mass velocities for Pe = 8 and Pe = 128 as a function of the squimers' velocity ration α.

2. *Target swim speed along self-propulsion direction*

Figure S2**c** presents effective swim speed $\langle \boldsymbol{U}_t \cdot \boldsymbol{e}_t\rangle$ of the target along its propulsion direction. Since the pursuer is aligned toward the center-of-mass, its self-propulsion

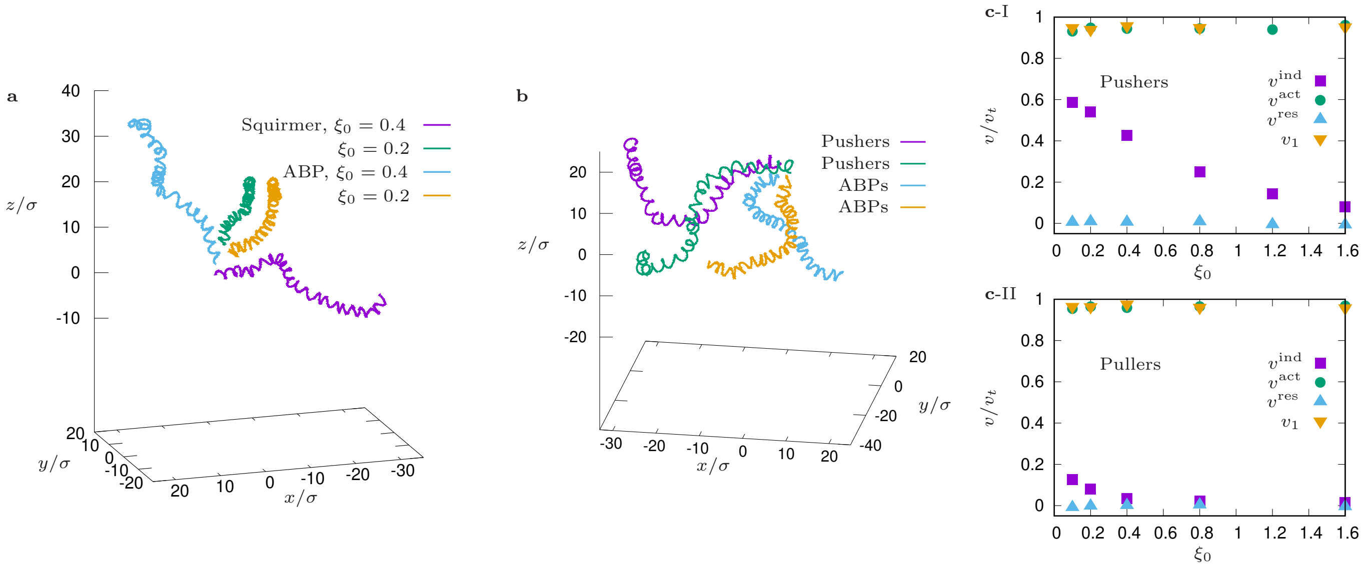

FIG. S3. **a** Helical trajectories for an individual squirmer and an individual ABP with chirality for $\mathrm{Pe} = 128$ and $\xi_0 = 0.2$, $\xi_0 = 0.4$. **b** Target trajectories for squirmer- and ABP-pairs for $\mathrm{Pe} = 128$, $\xi_0 = 0.2$, $\alpha = 1$, and $\Omega = 8\,\Omega^{\mathrm{hel}}$, where $\Omega^{\mathrm{hel}} \equiv \mathrm{Pe}/\sqrt{1+\xi_0^2}$ is the target angular velocity in units of D_R. **c** Average self-propulsion v^{act}, induced v^{ind}, and residual v^{res} velocities (Eq. (S37)) as well as v^{ind} of an individual chiral squirmer for (I) pushers and (II) pullers.

speed is almost identical to U_{cm}. The target dynamics to some extent decouples from the center-of-mass motion, because its propulsion direction experience thermal fluctuations, which are not compensated by active steering, and the pursuer not necessarily pushes in the direction of $\boldsymbol{e}_t$. As shown in Fig. S2**c**, the effective velocity of the target along $\boldsymbol{e}_t$ differs from the center-of-mass velocity. Yet, is higher than the prescribed value, i.e., $\langle \boldsymbol{U}_t \cdot \boldsymbol{e}_t \rangle / v_p > \alpha$, for $\alpha < 1$, as the target is pushed by the pursuer via hydrodynamic interactions and/or steric repulsion.

S-IV. HELICAL TRAJECTORY

A. Helical ABP

Considering an Brownian particle as a rigid body, a chiral active Brownian particle (cABP) can be realized by applying a constant angular velocity in the body-fixed frame. The equations of motion for an overdamped cABP are

$$\dot{\boldsymbol{r}} = v_0 \boldsymbol{e} + \sqrt{2D_T}\boldsymbol{\eta}_T, \tag{S32}$$

$$\dot{\boldsymbol{e}} = (\boldsymbol{\omega}_0 + \sqrt{2D_R}\boldsymbol{\eta}_R) \times \boldsymbol{e}, \tag{S33}$$

$$\dot{\boldsymbol{e}}_x = (\boldsymbol{\omega}_0 + \sqrt{2D_R}\boldsymbol{\eta}_R) \times \boldsymbol{e}_x, \tag{S34}$$

$$\dot{\boldsymbol{e}}_y = (\boldsymbol{\omega}_0 + \sqrt{2D_R}\boldsymbol{\eta}_R) \times \boldsymbol{e}_y, \tag{S35}$$

where $\boldsymbol{e}_x$, $\boldsymbol{e}_y$, and $\boldsymbol{e}_z = \boldsymbol{e}$ indicate the body-axes and $\boldsymbol{\omega}_0 = (C_{11}\boldsymbol{e}_x + \tilde{C}_{11}\boldsymbol{e}_y + C_{01}\boldsymbol{e})/R_{\mathrm{sq}}^3$ as for the squirmer (Eq. (7) of the main text). The values for C_{11}, $\tilde{C}_{11}$, and C_{01} are given in Eqs. (16) and (17) of the main text. The numerical solution of the Eqs. (S32)–(S35) is obtained via a quaternion representation, where

$$\dot{\boldsymbol{q}} = \frac{1}{2}\mathbf{Q}(\boldsymbol{q}) \cdot \begin{pmatrix} 0 \\ \boldsymbol{\omega}_0^b + \sqrt{2D_R}\boldsymbol{\eta}^b \end{pmatrix}. \tag{S36}$$

Note that $\ddot{\boldsymbol{q}}$ is irrelevant for overdamped ABPs. Example trajectories from simulations with a single cABP and a single squirmer with $\mathrm{Pe} = 128$ are shown in Fig. S3**a** for $\xi = 0.2$ and 0.4. In addition, target trajectories for pursuer-target squirmer- and APB-pairs are present in Fig. S3**b**.

B. Hydrodynamic effects: induced velocity

The target velocity $\boldsymbol{U}_t$ can be decomposed into components along its propulsion direction, v^{act}, the vector connecting the pursuer and the target, v^{ind}, and orthogonal to these vectors, v^{res}, such that

$$\boldsymbol{U}_t = v^{\mathrm{act}}\boldsymbol{e}_t + v^{\mathrm{ind}}\boldsymbol{e}_c + v^{\mathrm{res}}\boldsymbol{e}_0, \tag{S37}$$

with $\boldsymbol{e}_0 \equiv \boldsymbol{e}_t \times \boldsymbol{e}_c / |\boldsymbol{e}_t \times \boldsymbol{e}_c|$. The self-propulsion v^{act}, induced v^{ind}, and residual v^{res} velocities are presented in Fig. S3**c**. Since $v^{\mathrm{res}} \approx 0$, the hydrodynamic flow field of the pursuer causes only an induced velocity v_{ind}. Thereby, the active velocity v^{act} is approximately 5% smaller than the prescribed value v_t. A similar effect for the active velocity is observed in simulations of an individual chiral squirmer (v_1), confirming that the presence of a pursuer leaves the self-propulsion velocity unchanged.

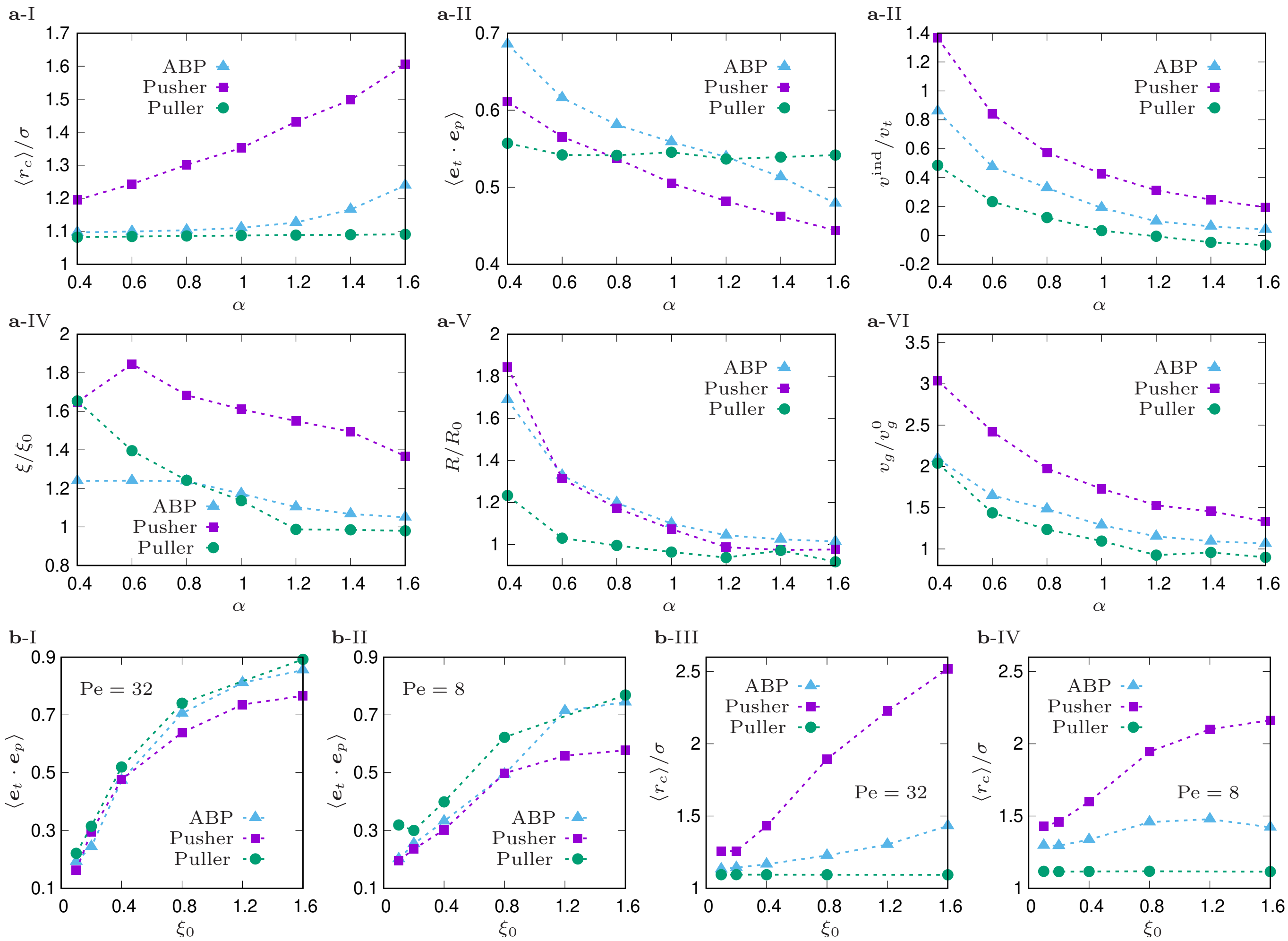

FIG. S4. **a** (I) Average pursuer-target distance $\langle r_c \rangle$, (II) orientation alignment parameter of the propulsion directions $\langle \boldsymbol{e}_t \cdot \boldsymbol{e}_p \rangle$, (III) induced velocity along the target propulsion direction v^{ind}, (IV) helix slope ξ, (V) helix radius R, and (VI) effective swim velocity v_g along the helix axis as a function of the velocity ratio α for the of pursuit dynamics on a helical trajectory with $\xi_0 = 0.4$. The pursuer touches the target for $\langle r_c \rangle/\sigma \approx 1.1$. **b** (I, II) Orientation alignment parameter of the propulsion directions $\langle \boldsymbol{e}_t \cdot \boldsymbol{e}_p \rangle$ and (III, IV) average distance $\langle r_c \rangle$ for Pe = 32 and Pe = 8, respectively.

C. Dependence on the pursuer propulsion speed

Figure S4**a** displays results for the pursuit of the chiral target moving on a helical trajectory as a function of the relative speed α, where the target self-propulsion speed v_t is fixed to maintain the geometry of the helical trajectory. As shown in Fig. S4**a**-I, the distance increases as the pursuer speed decreases (or α increases), except for pullers, where the target and the pursuer are touching due to hydrodynamic attractions. The average alignment $\langle \boldsymbol{e}_t \cdot \boldsymbol{e}_p \rangle$ of the propulsion directions decreases as α increases for pushers and ABPs, while pullers exhibit a rather persistent orientation (Fig. S4**a**-II).

Pronounced hydrodynamics effects appear for the induced velocity $\boldsymbol{v}^{\mathrm{ind}}$ (Fig. S4**a**-III). At small α, the faster pursuer compared to the target pushes the target either by steric interactions (ABPs, pullers with $\langle r_c \rangle/\sigma \approx 1.1$) or hydrodynamically (pushers). At large α, the slower pusher and ABP pursuer still pushes the target as evident by the velocities $v^{\mathrm{ind}} > 0$; they take a shorter path than the target. In case of pullers, the target is indeed pulled back by the slow pursuer ($v^{\mathrm{ind}} < 0$). The geometry of the resultant target trajectory is characterized by an effective slope ξ and radius R. The values of R and H are calculated via Eqs. (7), (18) and (19) of the main text. As depicted in Figs. S4**a**-IV and S4**a**-V, the slope for $\alpha < 1$ is larger than that of the single helix trajectory (ξ_0) for all pairs, i.e., the helical trajectory is more extended by the pushing pursuer. This is particularly pronounced for pusher pairs. The slope changes rather weakly for ABP and puller pairs with increasing α, whereas a significant reduction is obtained for pullers. At $\alpha < 1$, the radius of the helix is larger than the target value R_0, indicating a substantial pushing effect of the pursuer on the target helical trajectory. R decreases with increasing α and $R \approx R_0$ for $\alpha \approx 1.5$. Figure S4**a**-

VI, presents effective swimming velocity v_g of the pairs along the axis of the helical trajectory, where v_g is determined via as $v_g \equiv H/T_0$, where T_0 is the period of one helix turn. The pair velocity is (substantially) enhanced for any swimmer combination and decreases with increasing α. Even for $\alpha > 1.5$ pusher pairs move fast along the helix axis, because the pursuer takes a shorter path and is still able to push the target despite moving slower.

Figure S4**b** presents the average of the relative alignment $\langle \boldsymbol{e}_t \cdot \boldsymbol{e}_p \rangle$ and the mean pursuer-target distance $\langle r_c \rangle$ for $\alpha = 1.0$ as a function of ξ_0 (cf. Fig. 3**b** and **c**).

S-V. PROPULSION DIRECTION ALIGNMENT

A. Order parameter

To illustrate self-steering without speed adaptation, i.e., $\kappa = 0$ (Eq. (20)), Fig. S5**a** displays the orientational alignment parameter $\langle \boldsymbol{e}_t \cdot \boldsymbol{e}_p \rangle$ as a function of the maneuverability. The alignment parameter increase with increasing Ω and approaches approximately unity for $\Omega > 10^2$. However, it is independent of Pe and the swimmer type (pushers, pullers, and ABPs). Moreover, simulations show that the target and pursuer squirmers move independently. Thus, without any further adaptation scheme, e.g., speed adaptation, no cooperative motion emerges and hydrodynamic effects are negligible at this low microswimmer density.

B. Near-field hydrodynamic effects

1. *Instability*

Hydrodynamic interactions between two squirmers are asymptotically repulsive at long times, even if the transient motion can be rather long [12, 13]. Thermal fluctuations accelerate this behavior [8, 15], rendering cooperative motion of initially aligned squirmers unstable. While a deviation from the parallel arrangement is essentially suppressed due to the self-steering of pursuer, cooperative motion of persistently aligned squirmers ($\Omega \gtrsim 10$ in Fig. S5**a**) is still unstable.

Neglecting hydrodynamics, translational thermal noise disturbs the coherent motion of a target and a pursuer, even when they are perfectly aligned. Hydrodynamic attraction might stabilize the cooperative motion. For pushers, as hydrodynamic forces are attractive in the side-by-side configuration, a target and a pursuer may move in parallel, see Fig. S5**b**-I for illustration. However, rotational fluctuations of the target and hydrodynamic interactions still destabilize such configurations. Specifically, while the self-steering of the pursuer completely suppresses a divergence of the relative orientation, even a perfectly synchronized rotation of two squirmers affects their relative position in the direction of motion. For

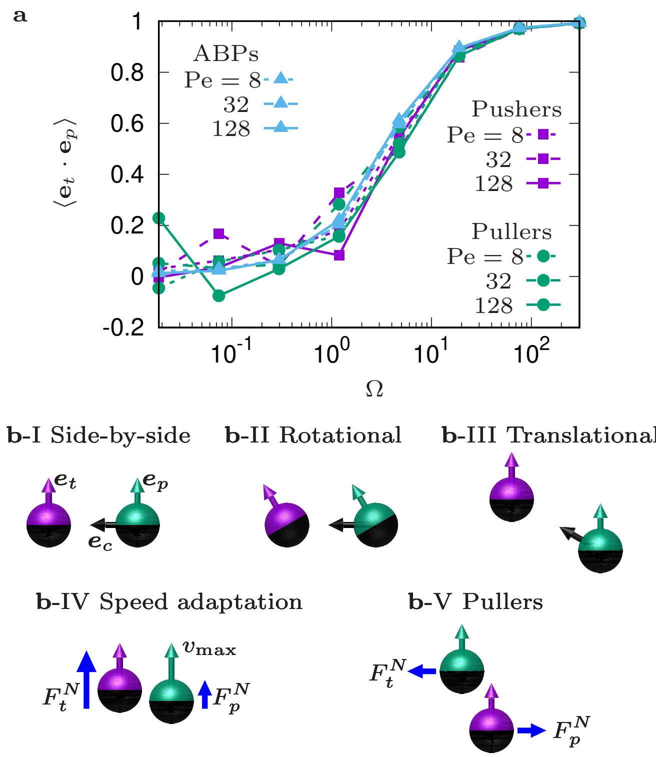

FIG. S5. **a** Orientational alignment parameter $\langle \boldsymbol{e}_t \cdot \boldsymbol{e}_p \rangle$ of the relative alignment of the target and pursuer propulsion directions as a function of maneuverability Ω for pushers, pullers, and ABPs and the indicated Péclet numbers. **b** Illustration of hydrodynamic instability and speed adaptation for a pusher pursuer- (green-black sphere) and target-pair (purple-black sphere). (I) A schematics of a side-by-side configuration, where $\boldsymbol{e}_t = \boldsymbol{e}_p \perp \boldsymbol{e}_c$. Hydrodynamic interactions between the squirmers are attractive. Both, synchronized (II) rotational and (III) translational fluctuations result in configurations deviating from the side-by-side configuration (I). (IV) Such deviations lead to a dispersion in hydrodynamic forces (blue arrows next to squirmers), i.e., $F_t^N > F_p^N$ in this case, and consequently, a configurational instability. To compensate for the force disparity, we introduce a speed adaptation, which allows the pursuer to swim faster than the target ($v_{\max} > v_t$). (V) For aligned pullers, hydrodynamic forces in the transverse direction destabilize head-to-tail configurations.

instance, a $\pi/2$ rotation changes a side-by-side arrangement to head-to-tail one, see Fig. S5**b**-II for illustration. Such a change in relative positions implies effective hydrodynamic forces in the propulsion direction, which are repulsive for pushers and thereby lead to a separation of pursuer and target even in configurations favored by their swimming type. Apparently, translation fluctuations also introduce similar configurational changes, as shown in Fig. S5**b**-III.

A more quantitative insight is achieved by the near-field approximation of the hydrodynamic interactions [12]. Assuming perfect align of the propulsion directions, i.e., $\boldsymbol{e}_t \parallel \boldsymbol{e}_p \equiv \boldsymbol{e}$, the near-field force in the $\boldsymbol{e}_c$

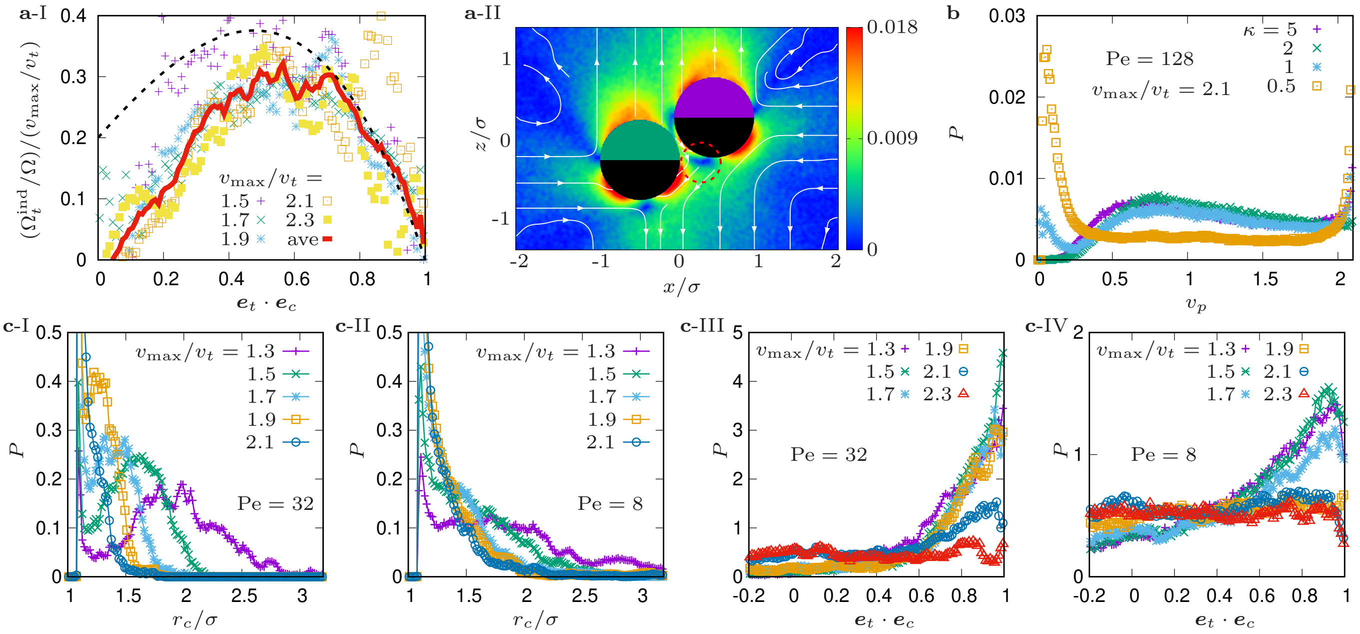

FIG. S6. **a** (I) Hydrodynamically induced angular velocity $\Omega^{\rm ind}$ as a function of the product $\boldsymbol{e}_t \cdot \boldsymbol{e}_c$ (symbols) for various maximum velocities. The black dotted line represents the asymptotic near-field approximation of Eq. (S42), multiplied by an constant to match the near-field approximation at large arguments. The red solid line shows the average induced angular velocity over all $v_{\max}$. (II) Flow-field computed from configurations with $r_c/\sigma < 8/6$ and $0.4 < \boldsymbol{e}_t \cdot \boldsymbol{e}_c < 0.6$. The target flow-field at the region highlighted by a red dashed circle is significantly modified and gives rise to the induced angular component $\Omega^{\rm ind}$. **b** Probability distribution function of the pursuer velocity for various κ. **c** Probability distribution function of the pursuer-target distance for (I) Pe = 32 and (II) Pe = 8, and probability distribution function of the relative orientation $\boldsymbol{e}_t \cdot \boldsymbol{e}_c$ for (III) Pe = 32 (III) and (IV) Pe = 8.

direction is on the order of

$$F_c = O(|\ln d|), \tag{S38}$$

where $d \equiv r_c - \sigma$ denotes the small gap distance between the target and pursuer. In the $\boldsymbol{e}_0$ direction perpendicular to both $\boldsymbol{e}$ and $\boldsymbol{e}_c$, i.e. $\boldsymbol{e}_0 \equiv \boldsymbol{e} \times \boldsymbol{e}_c / |\boldsymbol{e} \times \boldsymbol{e}_c|$, the hydrodynamic force must vanish due to symmetry. In the direction along $\boldsymbol{e}_n \equiv \boldsymbol{e}_0 \times \boldsymbol{e}_c$, the hydrodynamic forces on the target and the pursuer are [12]

$$F_t^N \approx -\frac{3\eta\pi\sigma v_0}{4}(\boldsymbol{e}\cdot\boldsymbol{e}_n)(1-\beta\boldsymbol{e}\cdot\boldsymbol{e}_c)\ln d, \tag{S39}$$

$$F_p^N \approx -\frac{3\eta\pi\sigma v_0}{4}(\boldsymbol{e}\cdot\boldsymbol{e}_n)(1+\beta\boldsymbol{e}\cdot\boldsymbol{e}_c)\ln d, \tag{S40}$$

where $\boldsymbol{e}\cdot\boldsymbol{e}_n = -|\boldsymbol{e}\times\boldsymbol{e}_c|$ in terms of $\boldsymbol{e}$ and $\boldsymbol{e}_c$. We also note that, when $\boldsymbol{e} = \boldsymbol{e}_c$, F_c is the only non-zero component due to symmetry.

Considering a side-by-side configuration, $\boldsymbol{e}_n = \boldsymbol{e}_t = \boldsymbol{e}_p$, and introducing a small deviation in the configuration of the form $\boldsymbol{e}_c' = \boldsymbol{e}_c + \epsilon\boldsymbol{e}_n$, see Fig. S5**b**-IV. For stability of the side-by-side configuration, the target must swim slower than the pursuer for $\epsilon > 0$ and faster for $\epsilon < 0$. The hydrodynamic forces exerted on the target and the pursuer by the respective other squirmer in the $\boldsymbol{e}_n$ direction are given in Eqs. (S39) and (S40). To the leading order, the difference between the forces in this geometry is

$$F_t^N - F_p^N \approx \frac{3\eta\pi\sigma v_0}{2}\beta\epsilon\ln d. \tag{S41}$$

Since $\beta < 0$ for pushers and $\ln d < 0$ for small gap distances, $F_t^N > F_p^N$ for $\epsilon > 0$ indicating that the target moves faster than the pursuer, which contradicts the necessary condition for stability. The same contradiction applies to $\epsilon < 0$. Hence, the distance between the target and pursuer in their propulsion direction grows, which renders side-by-side configurations unstable for pusher pairs with $\alpha = 1$. To compensate the force disparity, we introduce a speed adaptation, namely an additional active force in the longitudinal direction, which accelerates the pursuer for $\epsilon > 0$ and slows down for $\epsilon < 0$.

For pullers, the same argument leads to the conclusion that the head-to-tail configuration is unstable due to hydrodynamic forces in the transverse direction (Fig. S5**b**-V), in spite of hydrodynamic attraction in the longitudinal direction.

2. *Near-field hydrodynamic torque*

Self-steering and speed adaptation imply affects of the pursuer on the target dynamic by near-field hydrodynamics. Specifically, the torque

$$\boldsymbol{T}_t^N \approx \frac{\eta\pi\sigma^2}{4}(\boldsymbol{e}\times\boldsymbol{e}_c)(\boldsymbol{e}\cdot\boldsymbol{e}_n)(1-\beta\boldsymbol{e}\cdot\boldsymbol{e}_c)\ln d \quad \text{(S42)}$$

is exerted on the target by a pursuer [12]. Torques exerting on a pursuer are less significant because the pursuer can nearly cancel the torques by self-steering for large enough maneuverability.

The near-field effects on the pusher pair are illustrated Fig. S6**a** for configurations with $r_c/\sigma = 4/3$. As shown in Fig. S6**a**-I for the induced angular velocity Ω^{ind}, the simulation data exhibit a similar behavior to the theoretically prediction, except for small $\boldsymbol{e}_t\cdot\boldsymbol{e}_c$. Here, the speed adaptation, namely acceleration when the pursuer is behind and slow-down when the pursuer overshoots the target, seems to affect hydrodynamic interactions significantly and to modify the dynamics. As the target and pursuer are touching in this regime, Stokeslets due to steric repulsion may also be contribute and lead to deviations from the near-field approximation of the squirmer flow field. Figure S6**a**-II, presents the flow-field profile for $0.4 < \boldsymbol{e}_t\cdot\boldsymbol{e}_c < 0.6$, where Ω^{ind} assumes the maximum in Fig. S6**a**-I.

C. Relaxation time constant

For an efficient speed adaptation, the value of κ needs to be large enough such that the pursuer adjusts its propulsion speed quickly. As shown in Fig. S6**b**, the distribution function for the propulsion velocity v_p exhibits two peaks at $v_p \approx 0$ and $v_p \approx v_{\max}$ for $\kappa = 0.5$, demonstrating that the pursuer is either located behind the target or overshooting the target, but it hardly moves next to the target in contrast to $\kappa \geq 1$.

D. Péclet number

Probability distribution functions of the pursuer-target distance r_c and the orientation of the target propulsion direction along the vector connecting the squirmer centers $\boldsymbol{e}_t\cdot\boldsymbol{e}_c$ are presented in Fig. S6**c** for the Péclet numbers $\mathrm{Pe} = 8$ and 32. While the distribution function $P(r_c)$ for $\mathrm{Pe} = 32$, $\mathrm{Pe} = 128$ and the various $v_{\max}$ exhibit the same characteristics with a peak at intermediate r_c (Fig. S6**c**-I), the $P(r_c)$ curves for $\mathrm{Pe} = 8$ show a rather monotonic decrease as r_c increases (Fig. S6**c**-II). The distribution function $P(\boldsymbol{e}_t\cdot\boldsymbol{e}_c)$ for $\mathrm{Pe} = 8$ and $\mathrm{Pe} = 32$ shows no peaks (Figs. S6**c**-III and IV), in sharp contrast to the distribution for $\mathrm{Pe} = 128$ (Fig. 4**d** of the main text), where an additional peak develops at $\boldsymbol{e}_t\cdot\boldsymbol{e}_c \approx 0.2$ for large $v_{\max}$.

S-VI. SUPPLEMENTARY MOVIES

In all movies, the target and pursuer are represented by a purple-black and petrol-black sphere, respectively. Background fluid particles are not shown. All the movies show pursuit dynamics for 1.2×10^7 MPC steps, which correspond to the elapsed time of $t = 3.12/D_R$.

Movie 1: Pursuit on noisy straight trajectory for a puller target and a puller pursuer. In the movie, the pursuer and target keep touching each other. The puller pursuer slower than the target ($\alpha = 1.2$) is able to keep track of the target, due to hydrodynamic attractions between pullers in the head-to-tail configuration. $\mathrm{Pe} = 128$, $\Omega = 512$.

Movie 2: Pursuit on noisy straight trajectory for a pusher target and a pusher pursuer. As hydrodynamic effects are repulsive for pushers in the head-to-tail configuration, only a pursuer faster than its target can perform stable pursuit ($\alpha = 0.8$ in this movie). Moreover, the pursuer and target remain separated in sharp contrast to the pullers. $\mathrm{Pe} = 128$, $\Omega = 512$.

Movie 3: Pursuit on helical trajectory for pullers. While the pair exhibits stable touching configurations, their propulsion directions are not aligned in contrast to the pursuit on straight trajectories, thereby deviating from the head-to-tail configuration. Moreover, the pursuer moves on a helical trajectory with a radius smaller than that of the target trajectory, which indicates a shorter traveled distance for the pursuer. $\mathrm{Pe} = 128$, $\Omega = 951$, $\alpha = 1.0$, $\xi_0 = 0.4$.

Movie 4: Pursuit on helical trajectory for pushers. The pursuer with the same prescribed speed as the target ($\alpha = 1$) manages to keep track of the target, while maintaining a finite distance from the target. $\mathrm{Pe} = 128$, $\Omega = 800$, $\xi_0 = 0.8$.

Movie 5: Pursuit by a pusher pursuer through the propulsion direction alignment and speed adaptation for small $v_{\max}$ ($v_{\max} = 1.3$ in this movie). The pursuer follows the target in front with a finite distance in the head-to-tail configuration. Occasionally, the pursuer reaches the side of the target. $\mathrm{Pe} = 128$, $\Omega = 75.9$, $\kappa = 1$.

Movie 6: Cooperative circular swimming of pushers by propulsion direction alignment and speed adaptation. The pursuer swims next to but behind the target. Hydrodynamic torques induced by the pursuer rotate the target to the opposite direction to the pursuer. Mostly, the pursuer is swimming faster than the target due to the speed adaptation ($v_{\max}/v_t = 1.7$ in this case). $\mathrm{Pe} = 128$, $\Omega = 75.9$, $\kappa = 1$.

[1] A. Lamura, G. Gompper, T. Ihle, and D. M. Kroll, Europhys. Lett. **56**, 319 (2001).
[2] A. Malevanets and R. Kapral, J. Chem. Phys. **110**, 8605 (1999).
[3] G. Gompper, T. Ihle, D. M. Kroll, and R. G. Winkler, Adv. Polymer Sci. **221**, 1 (2009).
[4] H. Noguchi and G. Gompper, Phys. Rev. E **78**, 016706 (2008).
[5] M. Theers and R. G. Winkler, Soft Matter **10**, 5894 (2014).
[6] C. Huang, A. Chatterji, G. Sutmann, G. Gompper, and R. Winkler, J. Comput. Phys. **229**, 168 (2010).
[7] C.-C. Huang, A. Varghese, G. Gompper, and R. G. Winkler, Phys. Rev. E **91**, 013310 (2015).
[8] M. Theers, E. Westphal, G. Gompper, and R. G. Winkler, Soft Matter **12**, 7372 (2016).
[9] I. P. Omelyan, Phys. Rev. E **58**, 1169 (1998).
[10] K. Qi, E. Westphal, G. Gompper, and R. G. Winkler, Phys. Rev. Lett. **124**, 068001 (2020).
[11] J. T. Padding, A. Wysocki, H. Löwen, and A. A. Louis, J. Phys.: Condens. Matter **17**, S3393 (2005).
[12] T. Ishikawa, M. P. Simmonds, and T. J. Pedley, J. Fluid Mech. **568**, 119 (2006).
[13] I. Llopis and I. Pagonabarraga, J. Non-Newton. Fluid Mech. **165**, 946 (2010).
[14] J. Clopés, G. Gompper, and R. G. Winkler, Soft Matter **16**, 10676 (2020).
[15] I. O. Götze and G. Gompper, Phys. Rev. E **82**, 041921 (2010).